A Novel Approach for the Modeling of Electromagnetic Forces in Air-Gap Shunt Reactors

Hung Bui Duc
School of Electrical Engineering
Hanoi University of Science and Technology
Vietnam
hung.buiduc@hust.edu.vn

Tu Pham Minh
School of Electrical Engineering
Hanoi University of Science and Technology
Vietnam
tu.phaminh@hust.edu.vn

Tuan Phung Anh
School of Electrical Engineering
Hanoi University of Science and Technology
Vietnam
tuanphunganh1@hust.edu.vn

Vuong Dang Quoc
School of Electrical Engineering
Hanoi University of Science and Technology
Hanoi, Vietnam
vuong.dangquoc@hust.edu.vn

Abstract-Shunt reactors are usually used in electrical systems to imbibe reactive powers created by capacitive powers on the lines when the system is operating on low or no loads. Moreover, they are also used to balance reactive powers and maintain the stability of a specified voltage. In general, the air gaps of a magnetic circuit shunt reactor are arranged along the iron core to reduce the influence of fringing and leakage fluxes. Therefore, non-magnetic materials made of ceramics or marbles are often used in air gaps to separate the iron core packets. The direction of the fringing flux is perpendicular to the laminations, so the core packets of the shunt reactor are generally made from radially laminated silicon steels. Due to the alternating electromagnetic field through the core, a periodically altered electromagnetic force is produced between the core packets, tending to compress the ceramic spacers. This electromagnetic force causes vibration and noise in the core. In this research, a finite element approach based on the Maxwell stress tensor was developed to compute the magnetic flux density and the electromagnetic forces appearing in a shunt reactor.

Keywords-shunt reactor; air gaps; magnetic flux density; electromagnetic force; Maxwell stress tensor

I. INTRODUCTION

A Shunt Reactor (SR) is an important component widely used in power transmission systems to improve stability and efficiency. Parasitic capacitance occurs in a line when the system is working under low or no load. Especially for a long line, its value is very large and leads to a voltage increase, causing an overvoltage at its end. Hence, to maintain voltage stability according to the regulations and balance the reactive power in electrical systems, the SR is proposed to absorb the excess reactive power created by the line capacitance [1-4]. In addition, in order to reduce the magnetic flux and to avoid the saturation of the magnetic circuit, air gaps are added in the iron core of the SR to increase the reluctance values. On the other hand, fringing fluxes appear around the air gaps [6-9],

increasing the winding inductance and causing nonuniform magnetic fields in the iron core packets of the SR. Nonmagnetic materials such as ceramic or marble are often used in air gaps to separate the iron core packets. The fringing flux departs and reenters the lamination perpendicularly, so the core packets of the SR are generally made from radially laminated silicon steels. Because of the alternating electromagnetic field through the core, a periodically altering electromagnetic force is produced between the core packets, tending to compress the ceramic spacers. The force on the core packets is a Maxwell force that causes vibration and noise. Maxwell forces are acting at twice the power frequency due to the sinusoidal flux passing through the windings at the power frequency.

Many researchers have investigated transient situations and magnetic fields in SR or calculated the air-gap reluctance and -inductance of winding for magnetic circuits [6-12]. In [13], a method was introduced to calculate the leakage fields in air-core reactors using a 3D reluctance network. Testing problems of gapped-core reactors were presented in [14, 15]. Some researchers investigated the temperature field distribution [16, 17]. In this research, a Finite Element Method (FEM) based on Maxwell stress tensor theory [18] was developed for an iron core gapped SR to compute the magnetic flux density and the electromagnetic force on the core packets. These fields are the inherent reason for the vibration and noise and tend to compress the ceramic spacers.

II. METHODOLOGY

A. The Structure of a Gapped-Core Shunt Reactor

The structure of an SR is illustrated in Figure 1. The mid limb with the non-magnetic gaps is enclosed by the winding. The winding is also enclosed by a frame of core steel providing the return path for the magnetic field. Three single-phase SRs are connected to provide a three-phase transmission line. A

Corresponding author: Hung Bui Duc

three-phase SR can also be used, having 3 or 5 limbed cores. Figure 1(b) shows a three-limbed core SR having a strong magnetic coupling between the 3 phases. A 5-limbed core is shown in Figure 1(c), where the phases are magnetically independent due to the enclosing magnetic frame formed by the two yokes and the two unwound side-limbs. The gapped core limbs are built of core packets. The core packet type is further classified into parallel and radially laminated core types by the core packet laminating methods. The parallel laminated core type has steel plates in parallel in the same direction as the power transformer core, and the radially laminated core type is constructed as a cylindrical core packet by laminating steel plates in the radial direction arranged in a wedge-shaped pattern [14]. The core packet is filled with epoxy resin and molded into one solid unit.
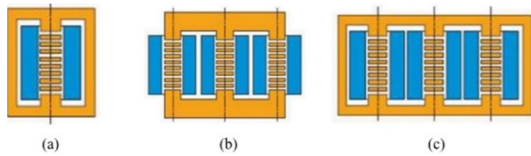
Fig. 1.   Modeling of the shunt reactor: (a) single-phase, (b) 3-phase 3-limbed core, (c) 3-phase 5-limbed core [6].

The vibration in the SRs is usually higher than in transformers as a result of the magnetic forces between the consecutive core packets. Therefore, the core is designed to eliminate excessive vibrations. The non-magnetic gaps are established by using cylindrical spacers to take the large magnetic forces appearing between the discs in a gapped core SR. The height of the distance spacer is equal to the height of the air gap. The core packets are stacked and cemented together to form a core limb column. Dimensional stability and core tightness can be fixed by an epoxy impregnated polyester material and a fiberglass cloth of a few millimeters between the last limb packet and the top/bottom yoke. The yokes and side limbs, normally with a rectangular cross-section, make up the magnetic circuit.

B. Parameters of the Shunt Reactor

A single-phase SR of 35MVAr ($500/\sqrt{3}$kV and 50Hz) was considered to calculate the electromagnetic force in the core packets. A simple model of this single-phase SR is shown in Figure 2. The volume of the air gaps was determined by the equations describing the magnetic circuit model. It should be noted that this volume depends on the main parameters of the shunt reactor, i.e. reactive power, magnetic inductance, winding inductance, frequency, and energy storage in the winding space air gap. Iron materials have usually a high magnetic permeability ($\mu=\mu_r.\mu_0$) compared to the air gap permeability (μ_0). Therefore, the reluctance of the magnetic core is very small, compared to the reluctance of the air gaps, and can be neglected in the equivalent magnetic circuit. In addition, the winding resistance is normally very small compared to the inductance and can be neglected when defining the parameters of the electric circuits. From the relationship between the Magnetomotive Force (MMF), magnetic flux, and reluctances of the magnetic circuit, the magnetic flux density on the core can be determined via the reactive power and the volume of the air gap as:

$$B_m = \sqrt{\frac{Q}{\frac{\pi}{\mu_0}.f.V_g}} \quad (1)$$

where B_m, V_g, and μ_0 are the maximum flux density, the air gap volume, and air permeability respectively. The obtained results of the SR of 35MVAr are shown in Table I [10]
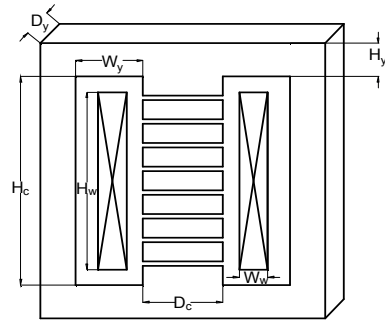
Fig. 2.   Model of the shunt reactor.

TABLE I.   SR RESULTS BY THE ANALYTIC METHOD

Parameters	Notation	Results
Reactive power	Q (MVAr)	35
Rated voltage	U (kV)	$500/\sqrt{3}$
Rated current	I (A)	121,24
Totalinductance	L (H)	7.5788
Core dimension	D_c (mm)	673
Height of core	H_c (mm)	1758
Total air gap length	l_g (mm)	363
Turn number	N (turn)	2166
Width of winding	W_w (mm)	248
Height of winding	H_w (mm)	1488

C. Calculation of the Electromagnetic Force

In the gapped core of the SR, vibrations can be very high due to the magnetic forces between the consecutive core packets. Thus, the ceramic spacers and any other gap materials should tolerate these forces without any significant shrinkage. The electromagnetic force acting on the core packets can be computed by either the Maxwell stress tensor approach or the virtual work method [20]. This force is given by:

$$F = \frac{\Delta W}{\Delta x} = \frac{1}{2}\frac{B^2}{\mu_0}A_c, \quad (2)$$

where A_c is the cross-sectional area, and Δx is the translation of a body. The surface force density is therefore given by:

$$F_S = \frac{F}{A_c} = \frac{1}{2}\frac{B^2}{\mu_0} \quad (\text{N/m}^2) \quad (3)$$

The higher the operating flux density, the higher the attractive force is. Therefore, the operation flux density is typically lower than the value used sometimes in power transformers. According to (2), it is necessary to increase the total volumic air gap to reduce the magnetic flux density. The force between the core packets can be calculated by (3) if the flux distribution is uniform. However, as the flux distribution in the SR is non-uniform, the finite element approach is generally applied with the virtual work principles. The magnetic flux density can be determined through the MMF and the air gap parameters as:

$$B = \frac{F}{A_c} = \mu_0 \frac{I.N}{l_g} \quad (4)$$

The surface force density can also be calculated by:

$$F_S = \frac{1}{2} \frac{\mu_0 I^2 N^2}{l_g} \quad (N/m^2) \quad (5)$$

The Maxwell stress tensor approach is widely used for computing electromagnetic forces. When ignoring the magnetostriction, the distribution of the magnetic forces in the core packets can be defined as:

$$F_v = -\frac{1}{2} H.H \nabla\mu \quad (6)$$

On the material surface, F_v can be written in terms of normal and tangential components as:

$$F_v = -\frac{1}{2}(H_t^2 + H_n^2) \nabla\mu$$
$$= -\frac{1}{2}\left(H_t^2 + \frac{B_n^2}{\mu^2}\right) \nabla\mu \quad (7)$$
$$= -\frac{1}{2}(H_t^2 \nabla\mu - B_n^2 \nabla v)$$

since $\frac{\nabla\mu}{\mu^2} = -\nabla v$, where reluctivity is $v = \frac{1}{\mu}$.

The force density at the surface can be defined as:

$$F_s = -\frac{1}{2}(H_t^2 (\mu_0 - \mu) - B_n^2 (v_0 - v))n \quad (8)$$

where *n* is the unit normal vector to the surface. In the gapped-core SR, the force density between two packets can be determined by (8), which when the fringing effect is negligible ($H_t=0$) becomes:

$$F_s = \frac{1}{2}(B_n^2 (v_0 - v))n \quad (9)$$

The reluctivity v of the core material in (9) is negligible. Thus, the magnitude of the force per unit area perpendicular to the surface can be expressed as:

$$F_S = \frac{1}{2}\frac{B^2}{\mu_0} \quad (N/m^2) \quad (10)$$

This force is a function of the square of the flux density. The higher the operating flux density, the higher the forces of attraction are.

D. Modeling of the Shunt Reactor via a Finite Element Approach

Maxwell's equations and the constitutive laws of the problem are written as [10-13]:

$$\nabla \times E = -\frac{\partial B}{\partial t} \quad (11)$$

$$\nabla \bullet B = 0 \quad (12)$$

$$\nabla \times H = J + \frac{\partial D}{\partial t} \quad (13)$$

$$B = \nabla \times A \quad (14)$$

The value of the magnetic flux density *B* corresponding to the magnetic field intensity *H* is:

$$B = \mu H \quad (15)$$

The magnetization forces were calculated by applying the Maxwell stress tensor locally. The Maxwell stress tensor for magnetic fields is a 3×3 matrix and has a unit of N/m²:

$$T = \begin{bmatrix} B_x H_x - \frac{1}{2}BH & B_x H_y & B_x H_z \\ B_y H_x & B_y H_y - \frac{1}{2}BH & B_y H_z \\ B_z H_x & B_z H_y & B_z H_z - \frac{1}{2}BH \end{bmatrix} \begin{bmatrix} n_x \\ n_y \\ n_z \end{bmatrix} \quad (16)$$

This is also a suitable approach for computing the force distributions. The divergence of the stress tensor f_v is defined by the volume force density in (16a), while the volume force is defined in (16b):

$$f_v = \nabla \cdot T \quad (16a)$$

$$F_v = \int_v \nabla \cdot T dv \quad (16b)$$

The force on the surface of the core packets can be obtained by:

$$F_S = \int_S T dS \quad (17)$$

The tangential F_t and the normal F_n components of the force *F* per unit area on an elemental surface can be expressed in terms of the tangential and normal field components as:

$$F_t = B_n H_t \quad (18a)$$

$$F_n = \frac{1}{2}\left(\frac{1}{\mu_0}B_n^2 - \mu_0 H_t^2\right) \quad (18b)$$

Both the normal component of *B* and the tangential component of *H* should be determined. In this part, the FEM was used to determine the modeled SR parameters, utilizing the Ansys Maxwell software [20]. The accuracy and the validity of FEM have been proven in recent studies [10, 12, 19]. Due to the anisotropy of the magnetic properties, a set of 3D laminated coordinate systems was defined considering the anisotropy of magnetic properties for laminated silicon steel in the Rolling Direction (RD), the Transverse Direction (TD), and the Lamination Direction (LD). The models of all parts (yokes, core packets, windings) in the 3D coordinate system were created, and core packets are shown in Figure 3(a). Then, the lamination direction of the yokes and all core packets was chosen in the 3D laminated coordinate systems. The core packet of the SR was generally made from radially laminated silicon steels, as shown in Figure 3(c). The mapping between the laminated and the rectangular spatial coordinate systems is presented in Table II.

III. RESULTS AND DISCUSSION

The mapping distributions of the magnetic flux density in the SR core are presented in Figure 4. The magnetic flux density in the SR model is shown in Figure 4(a)-(b). The distribution of the magnetic flux density on a core packet, generally made from radially laminated silicon steels as Figure 3(c), is presented in Figure 4(c). The magnetic flux density is unevenly distributed, especially in the core packets. The magnetic flux density around the core's corner is larger than in its interior due to the characteristics of the SR, which has air gaps between the core packets to increase the reluctance of the magnetic circuit. However, the fringing flux around the air gaps

increases the magnetic flux around the iron core packets. Together with the fringing flux, it is directed to the laminated silicon steel in the transverse direction, which has worse magnetic properties than the rolling direction. The magnetic flux density along the lines Y1-Y2 and Y3-Y4 is shown in Figure 5.
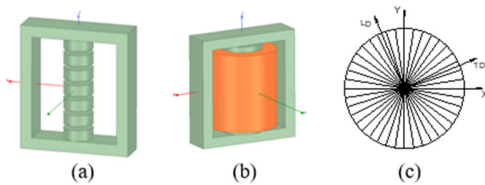
Fig. 3.   3D model of the single-phase SR and the radially laminated silicon steels.

TABLE II.   MAPPING BETWEEN THE TWO COORDINATE SYSTEMS

Part	RD	TD	LD
Core packets	z-axis	Perpendicular z-axis	Radial as a fan-shaped
Top and bottom yokes	x-axis	z-axis	y-axis
Side yokes	z-axis	x-axis	y-axis
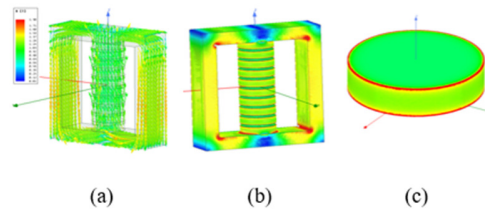
Fig. 4.   The magnetic flux density on the magnetic circuit and iron core packets.
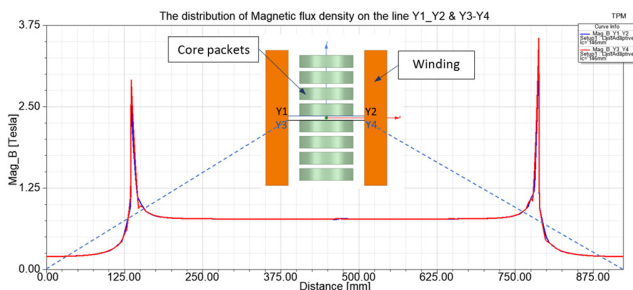
Fig. 5.   Magnetic flux density along the lines Y1-Y2 and Y3-Y4 on the surface of a core packet.

In the same way, the magnetic flux density around the outermost edge is highlighted in Figure 5. It is significantly larger than the rest, while this magnetic flux density is directly related to the electromagnetic force acting on the core packets. This electromagnetic force component will act on the ceramic plates that separate the core packets. The distribution of the force density on the surface of the core packets is shown in Figure 6. In the gapped-core SR, the magnetic force acts between the core packets like close electromagnets and can be interpreted as attractive forces that try to minimize the gap length. Due to the very high magnetic attraction forces between the core packets, the ceramic spacers and any other air gap material should tolerate these forces without any significant

shrinking. As shown in (14), these forces are a function of the square of the flux density, and thus the higher the operating flux density, the higher the forces of attraction are. The operating flux density is typically lower than the value usually used in power transformers. The cut values of the electromagnetic force density on the lines Y1-Y2 and Y3-Y4 on the core's surface are shown in Figure 7. It can be observed that these forces have the same value but in the opposite direction.
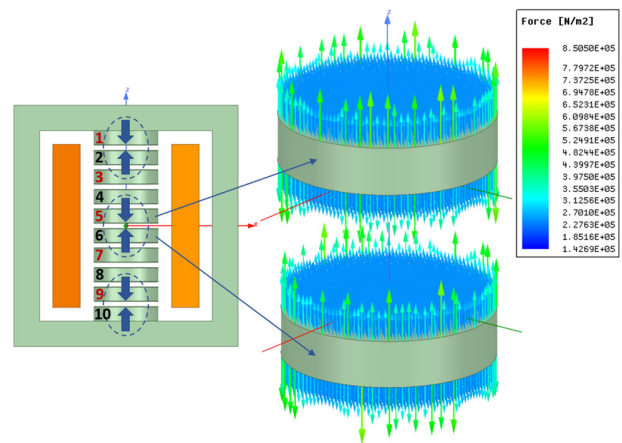
Fig. 6.   Distribution of the force density on the surface of the core packets.
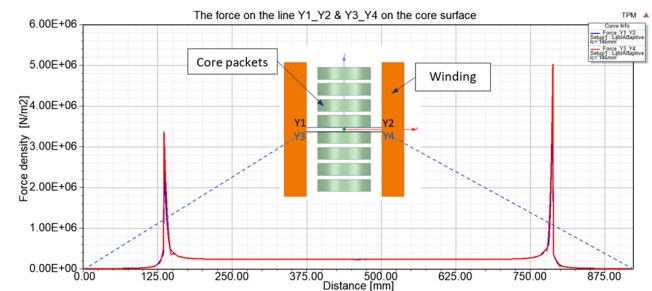
Fig. 7.   Distribution of force density along the lines Y1-Y2 and Y3-Y4 on the core surface.

Figures 5 and 7 show that the electromagnetic force results are similar to the magnetic field results. The electromagnetic force around the outermost edge is also significantly larger than in the rest. Figure 8 shows the post-processing normal forces acting on the top and bottom surfaces of the core packets. The positive normal forces are linked to the top surfaces of the core packets, whereas the negative normal forces are linked to the bottom surfaces. As shown in Figures 6 and 8, the forces acting on the top and bottom surfaces of each core packet are in the opposite directions and have approximately the same magnitude, resulting in a net force acting close to zero on each core packet. The ceramic spacers are in contact with the bottom surfaces of the upper core and the top surfaces of the lower core packets. Due to the two surface forces acting on the ceramic spacer in the opposite directions, these spacers suffer huge compression forces and should withstand approximately $257.5 kN/m^2$ or $26.3 Ton/m^2$. If the flux density on the iron cores is doubled, these forces will increase 4 times to over

$100Ton/m^2$. To withstand the very high forces acting on the ceramic spacers, their height has to be precisely uniform to ensure a uniform force distribution on all the ceramic spacers. Usually, the spacers are first glued to the core packet and then grinded to be equal. This result explains why during the design of shunt reactors, the flux density of their core should be smaller than the core of the power transformer, even using the same magnetic material.
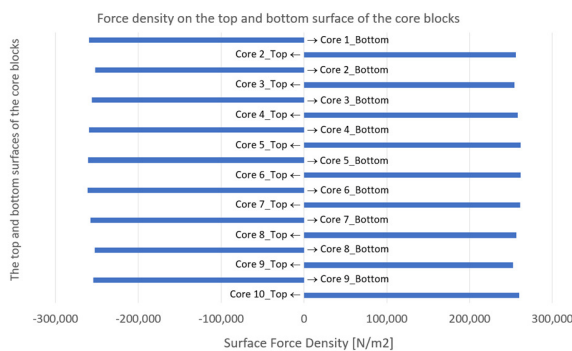
Fig. 8.   Force density distribution along the lines Y1-Y2 and Y3-Y4 on the surface of the core packets.

IV. CONCLUSION

This study investigated the electromagnetic forces on the core packets of a shunt reactor by both the virtual work method and the Maxwell stress tensor approach. In both methods, the normal forces are a function of the square of the flux density. Finite element approach, using Ansys Maxwell software, was applied to compute the magnetic flux density distribution and the normal surface forces density on the core packets. The forces acting on the top and bottom surfaces of each core packet are in opposite directions and have approximately the same magnitude, resulting in a near-to-zero net force acting on each core packet. However, as the surface forces act on the ceramic spacers in opposite directions, they become huge compression forces. Therefore, these results will be useful to researchers, design engineers, and manufacturers when choosing the appropriate magnetic flux density on the core in order to control the electromagnetic forces acting on the spacers between the core packets.

REFERENCES

[1]   G. Deb, "Ferranti Effect in Transmission Line," *International Journal of Electrical and Computer Engineering (IJECE)*, vol. 2, no. 4, 2012.

[2]   A. D. S. Sri, K. T. Devi, K. D. Raju, and B. Tanya, "Depiction and Compensation of Ferranti Effect in Transmission Line," *International Journal for Research in Applied Science and Engineering Technology*, vol. 6, no. 3, pp. 1522–1526, Mar. 2018, https://doi.org/10.22214/ijraset.2018.3234.

[3]   Z. Lubosny, "The Issues of Reactive Power Compensation in High-voltage Transmission Lines," *Acta Energetica*, vol. 23, no. 2, pp. 102–108, 2015, https://doi.org/10.12736/issn.2300-3022.2015210.

[4]   "Shunt Reactors For Medium and High Voltage Networks: From development to use," Siemens, Nurnberg, Germany, 2018.

[5]   H. Amreiz, A. Janbey, and M. Darwish, "Emulation of Series and Shunt Reactor Compensation," in *2020 55th International Universities Power Engineering Conference (UPEC)*, Sep. 2020, pp. 1–6, https://doi.org/10.1109/UPEC49904.2020.9209786.

[6]   L. M. Escribano, R. Prieto, J. A. Oliver, J. A. Cobos, and J. Uceda, "New modeling strategy for the fringing energy in magnetic components with air gap," in *APEC. Seventeenth Annual IEEE Applied Power Electronics Conference and Exposition (Cat. No.02CH37335)*, Mar. 2002, vol. 1, pp. 144–150, vol. 1, https://doi.org/10.1109/APEC.2002.989240.

[7]   S. Grebovic, N. Oprasic, and A. Balota, "Influence of Shunt Reactor Switching on Overvoltages in 400 kV Substation," in *2020 9th Mediterranean Conference on Embedded Computing (MECO)*, Jun. 2020, pp. 1–4, https://doi.org/10.1109/MECO49872.2020.9134116.

[8]   R. P. Hutahaean and G. Sianipar, "Transient analysis of 150 kV shunt reactor at Bulukumba Substation," in *Proceedings of the 2011 International Conference on Electrical Engineering and Informatics*, Jul. 2011, pp. 1–6, https://doi.org/10.1109/ICEEI.2011.6021818.

[9]   E. Kurt, A. Arabul, I. Senol, and F. K. Arabul, "An Investigation on Flux Density of Three Phase Distributed Air-Gap 3-5 Legged Shunt Reactor," in *Proceedings of The IRES 21st International Conference*, Amsterdam, Netherlands, Dec. 2015.

[10] T. P. Minh *et al.*, "Finite Element Modeling of Shunt Reactors Used in High Voltage Power Systems," *Engineering, Technology & Applied Science Research*, vol. 11, no. 4, pp. 7411–7416, Aug. 2021, https://doi.org/10.48084/etasr.4271.

[11] V. D. Quoc, "Robust Correction Procedure for Accurate Thin Shell Models via a Perturbation Technique," *Engineering, Technology & Applied Science Research*, vol. 10, no. 3, pp. 5832–5836, Jun. 2020, https://doi.org/10.48084/etasr.3615.

[12] V. D. Quoc, "Accurate Magnetic Shell Approximations with Magnetostatic Finite Element Formulations by a Subdomain Approach," *Engineering, Technology & Applied Science Research*, vol. 10, no. 4, pp. 5953–5957, Aug. 2020, https://doi.org/10.48084/etasr.3678.

[13] A. S. Nunes, P. Kuo-Peng, and M. G. Vanti, "Air Core Reactor Analysis Based on RNM Method," presented at the Compumag 2013, Budapest, Hungary, Jul. 2013.

[14] G. W. Alexander, R. H. Hopkinson, and A. U. Welch, "Design and Application of EHV Shunt Reactors," *IEEE Transactions on Power Apparatus and Systems*, vol. PAS-85, no. 12, pp. 1247–1258, Sep. 1966, https://doi.org/10.1109/TPAS.1966.291643.

[15] J. P. Vora, B. L. Johnson, and H. C. Barnes, "A New Shunt Reactor Principle Proved: Designed Data and Factory Test Results for Units Built on The Insulated Core Principle," *IEEE Transactions on Power Apparatus and Systems*, vol. PAS-92, no. 3, pp. 900–906, Feb. 1973, https://doi.org/10.1109/TPAS.1973.293655.

[16] F. Yuan *et al.*, "Thermal Optimization for Dry Type Air Core Reactor Base on FEM," in *2018 21st International Conference on Electrical Machines and Systems (ICEMS)*, Jul. 2018, pp. 1726–1730, https://doi.org/10.23919/ICEMS.2018.8549257.

[17] S. Magdaleno-Adame, R. Escarela-Perez, J. C. Olivares-Galvan, E. Campero-Littlewood, and R. Ocon-Valdez, "Temperature Reduction in the Clamping Bolt Zone of Shunt Reactors: Design Enhancements," *IEEE Transactions on Power Delivery*, vol. 29, no. 6, pp. 2648–2655, Sep. 2014, https://doi.org/10.1109/TPWRD.2014.2322994.

[18] S. V. Kulkarni and S. A. Khaparde, *Transformer Engineering : Design, Technology, and Diagnostics*, 2nd ed. Boca Raton, FL, USA: CRC Press, 2017.

[19] K. Dawood, G. Komurgoz, and F. Isik, "Modeling of Distribution Transformer for Analysis of Core Losses of Different Core Materials Using FEM," in *2019 8th International Conference on Modeling Simulation and Applied Optimization (ICMSAO)*, Apr. 2019, pp. 1–5, https://doi.org/10.1109/ICMSAO.2019.8880392.

[20] "Customer Support and Help Desk | Ansys." https://www.ansys.com/support (accessed Jan. 15, 2022).